Hovering rotor computations using an aeroelastic blade model

F. Dehaeze **G. N. Barakos**
G.Barakos@Liverpool.ac.uk
Department of Engineering
University of Liverpool
Liverpool, UK

ABSTRACT

In this paper, helicopter rotor blades are analysed in hover using computational fluid dynamics (CFD) coupled with a structural model. The method relies on a mesh deformation algorithm that allows for exchange of forces and deformations between a beam-based finite-element model and the fluid flow volume mesh. The method is demonstrated against experimental data, and the aerodynamic predictions appear to improve when the aeroelastic model is used. For all employed cases the flexibility of the method allows the CFD mesh deformation to be spread over the computational domain in a controlled fashion. The influence of the aeroelastic deformations on the blade loads was limited yet evident on the rotor performance. The lack of adequate test cases and experiments for validation of CFD/CSD methods is also highlighted.

NOMENCLATURE

$\vec{\mathbf{a}}$, $\vec{\mathbf{b}}$, $\vec{\mathbf{c}}$, $\vec{\mathbf{d}}$	vectors used for the projection of a fluid node on a triangular structural element, as defined in Paragraph 2.3
$\vec{\mathbf{a}}'$, $\vec{\mathbf{b}}'$, $\vec{\mathbf{c}}'$, $\vec{\mathbf{d}}'$	updated vectors $\vec{\mathbf{a}}$, $\vec{\mathbf{b}}$, $\vec{\mathbf{c}}$, $\vec{\mathbf{d}}$ after the structural deformation has been applied
a_l	lift slope factor (-)
c	chord length (m or ft)

Paper No. 3680. Manuscript received 19 November 2010, revised version received 12 July 2011, second revision received 12 October 2011, accepted 20 October 2011. A version of this paper was presented at the RAeS Applied Aerodynamics Conference, Bristol, UK, 27–28 July 2010 as paper no 3680.

https://doi.org/10.1017/S0001924000007107 Published online by Cambridge University Press

C_L sectional lift coefficient, $C_L = \frac{L_Z}{\frac{1}{2}\rho V_{sec}^2 c}$ (-)

C_P pressure coefficient, $C_P = \frac{P_\infty - P}{\frac{1}{2}\rho V_{sec}^2}$ (-)

C_Q rotor torque coefficient, $C_Q = \frac{Q}{\frac{1}{2}\rho\pi R^3 V_{tip}^2}$ (-)

C_q rotor sectional torque coefficient around the rotation axis, $C_q = \frac{L_M}{\frac{1}{2}\rho c^2 V_{tip}^2}$ (-)

C_T rotor thrust coefficient, $C_T = \frac{T}{\frac{1}{2}\rho\pi R^2 V_{tip}^2}$ (-)

C_t rotor sectional thrust coefficient $C_t = \frac{L_Z}{\frac{1}{2}\rho c V_{tip}^2}$ (-)

$\mathbf{d\vec{x}}$ displacement vector of the point $\vec{x}$,

$\mathbf{d\vec{x}}_1, \mathbf{d\vec{x}}_2, \mathbf{d\vec{x}}_3, \mathbf{d\vec{x}}_4$ displacement vectors of the face four corners

error convergence criterion of the spring analogy method

$\vec{F}_i, \vec{F}_v$ inviscid and viscous fluxes

$\vec{F}_i^v$ sum of the forces due to the surrounding springs on the *i*th vertex (N or lbf)

$\vec{F}_{ij}^v$ force on the *i*th vertex due to the spring between the *i*th and *j*th vertices (N or lbf)

FM rotor figure of merit $FM = \frac{\sqrt{\sigma} C_T^{\frac{3}{2}}}{2C_Q}$ (-)

k_{ij} stiffness of the spring between vertices *i* and *j* (N/m or lbf/ft)

L_M rotor moment loading around the blade pitch axis (N or lbf)

L_Z rotor loading along the span in the thrust direction (N/m or lbf/ft)

M local free-stream Mach number, $M = \frac{r}{R} M_{tip}$ (-)

M_{tip} Mach number at the tip of a blade due to the blade rotation (-)

N_b rotor blade number

n_i number of vertices linked by a spring to the *i*th vertex

$\vec{n}_i$ normal vector to the *i*th face of a cell

P pressure (N/m^2 or lbf/ft^2)

P_∞ free stream pressure (N/m^2 or lbf/ft^2)

Q rotor torque (N.m or lbf.ft)

R rotor radius (m or ft)

Re_{tip} Reynolds number at the tip of a blade based on the chord length and the hover speed at the blade tip $Re_{tip} = \frac{\rho_\infty c V_\infty}{\mu_\infty}$ with μ_∞ the dynamic viscosity of air at free stream conditions (-)

$R_{i,j,k}$ Flux residuals at cell (i, j, k)

$\vec{S}$ source term

S_1, S_2, S_3 corners of a structural element

s_1, s_2, s_3, s_4 stretching functions, defined in Equation 14

S_F sectional force coefficient, $S_F = \frac{L_Z}{\rho c V_{tip}^2}$ (-)

https://doi.org/10.1017/S0001924000007107 Published online by Cambridge University Press

Sk	cell skewness $Sk = max\ (\vec{n}_i \,.\, \vec{n}_j)$, $i \neq j$ (-)
Skr_{max}	Max skewness ratio $Skr_{max} = \frac{1-max(Sk_{deformed})}{1-max(Sk_{undeformed})}$ (-)
T	rotor thrust (N or lbf)
$\vec{u}_h$	local velocity field in the rotor-fixed frame of reference
$V(t)$	time dependent control volume
V_{sec}	velocity at a blade section due to the rotation, $V_{sec} = V_{tip}\frac{r}{R}$ (m/s^2 or ft/s^2)
V_{tip}	velocity at the blade tip due to the rotation (m/s^2 or ft/s^2)
$\mathbf{w_{i,j,k}}$	vector of conserved variables, discretise, on a CFD mesh
$\vec{\mathbf{w}}$	vector of the conserved variables $\vec{\mathbf{w}} = [\rho, \rho u, \rho v, \rho w, \rho E]^T$
$\vec{x}\,(\xi,\eta)$	co-ordinates of the point in the local face co-ordinates
$\vec{x}_1, \vec{x}_2, \vec{x}_3, \vec{x}_4$	co-ordinates of the four face corners (m or ft)
α,β,γ	coefficients used to define the CVT association between fluid nodes and structural elements after the structural deformation
α_{ij}	stiffness of the spring between vertices i and j (N/m or lbf/ft)
β_0	coning angle of the rotor (degrees)
γ_L	lock number (-)
λ	inflow factor (-)
$\vec{\delta}_i$	vector representing the displacement of the i-th block vertex in the spring analogy (m or ft)
$\overrightarrow{\delta_{i,new}}$	displacement of the i-th block vertex after the iterative update in the spring analogy (m or ft)
$\overrightarrow{\delta_{i,old}}$	displacement of the i-th block vertex before the iterative update in the spring analogy (m or ft)
ϕ_1^0,ϕ_2^0	blending functions in the η-direction defined in Equations 12 and 13
ψ_1^0,ψ_2^0	blending functions in the ξ-direction defined in Equations 10 and 11
ρ	air density (kg/m^3 or slug/ft^3)
σ	rotor solidity, $\sigma = \frac{N_b c}{\pi R}$(-)
θ_0	collective angle of the rotor (degrees)
ω	rotor rotational speed (rad/sec)
ξ,η	local co-ordinates on the face of a block

1.0 INTRODUCTION AND PREVIOUS WORK

Within rotorcraft research, comprehensive codes for rotor blade analysis usually include a structural model, an aerodynamic model based on lookup tables, free or prescribed wakes and combine these with flight mechanics tools for rotor trimming. Examples of such tools are CAMRAD[1,2] and HOST[3]. In this paper, the CFD is coupled with structural finite element models in an attempt to make the CFD prediction more realistic and add to the CFD some of the flexibility of comprehensive methods. There are three elements in this effort: the structural model, the coupling between fluid flow and structural deformations predictions, and the aeromechanics algorithm for the rotor trim.

In terms of structural modelling, the modal approach is the most popular. Potsdam *et al*[4] used CAMRAD for the UH-60A rotor in forward flight at various advance ratios, and Lim *et al*[5] and

https://doi.org/10.1017/S0001924000007107 Published online by Cambridge University Press

Biedron *et al*[6] used it for the HART-II rotor. Pahlke *et al*[7] dealt with the 7A and 7AD rotors at high advance ratios using the S4 code. Dietz *et al*[8] used HOST for the 7AD rotor as part of the GOAHEAD European project. Since in this work we are limited to hovering rotors, the modal approach is replaced by a finite-element method for aeroelastic coupling based on NASTRAN. This approach allows for the blade deformation to be estimated using structural properties and aerodynamic and centrifugal loads.

For the purpose of aeroelastic coupling, multiple approaches can be used. The most popular one is the loosely coupled approach[4,6,8,9] where the blade shape is updated every few time steps or even after the end of a rotor revolution. The blade deformation is computed as a linear combination of several eigenmodes. This approach was found to be more stable than the strongly coupled one by Altmikus *et al*[10]. Unlike loose coupling, strong coupling recomputes the blade shape at every time step. However, the strong coupling method allows for manoeuvring flight to be simulated as demonstrated by Sitaraman *et al*[11], this is not possible with a loose coupling strategy.

For hovering rotors, the loose coupling method has been used by Potsdam *et al*[12] within an unsteady flow simulation. However, neither strong nor weak coupling make full use of the properties of hovering rotors and therefore are not the most suitable in this case. The use of an unsteady simulation by Schmitz *et al*[13] and Yoon *et al*[14] proved more efficient.

Coupling methods for CFD/CSD simulations reported in the literature are summarised in Table 1. The mesh deformation methods are mainly based on spline interpolation of the deformed quarter chord line of the blade. The deformation is then spread at each radial section. However, more complex models based on 2D- or 3D-finite element models are being developed[14,16] and do not consider the blade sections to be rigid. Other deformation methods based on surface deformation propagation are therefore being proposed. An example of such method was presented by Thepvongs *et al*[17] The use of the multiquadric-biharmonic method also allowed for camber line deformations to be taken into account. A common theme shared by most of the methods shown in Table 1 is the use of overset grids. This leads to fewer requirements for the propagation of the blade surface deformations inside the flow domain. The method proposed in this work distinguishes between surface deformation, near-blade mesh deformation, and deformation of the flow domain away from the blades. This allows for compatibility with multi-block grids as described in Section 2.1.

In the open literature, most of the research studies on aeroelastic hovering rotors were conducted for model rotors, mainly the 7A/7AD and UH-60A rotors. The experiment of Lorber *et al*[18,19] for the hovering UH- 60A model rotor appear to be the most comprehensive in terms of available data, including surface pressure, wake and trim state. Unfortunately, the data does not include the structural deformations. In the case of the UH-60A, several CFD simulations were carried out to predict the flow and compared with this experiment. Wake and Baeder[20] used TURNS and their results compared well with the experimental pressure distribution on most of the blade. However, the predictions were not as accurate in the outer rotor part. Schmitz *et al*[13] simulated the model UH-60A rotor using the RANS UM-TURNS solver coupled with HELIX-IA to model the wake. Aeroelastic simulations were also carried out. However, the aeroelastic results were not presented in the paper due to the limited effect they had on the rotor figure of merit. For $C_T/\sigma = 0{\cdot}170$, their predictions were good on the main part of the blade, however, the outer part of the blade did not compare well with experimental results, particularly for the induced torque. As a result, the figure of merit was over predicted. The predictions from Yoon *et al*[14] showed that the main consequence of the structural deformation was to decrease the loading at the tip and increase the loading in the inner part of the blade.

https://doi.org/10.1017/S0001924000007107 Published online by Cambridge University Press

Table 1
CFD/CSD coupling and mesh deformation methods

Author	Structural model	CFD model	Blade surface deformation method	Volume grid deformation method	Coupling strategy
Potsdam, 2004[12]	CAMRAD-II (non-linear beam finite elements)	OVERFLOW-D (RANS solver, structured overset grids)	Cubic spline interpolation from the quarter-chord line deformation	Cubic spline interpolation from the quarter-chord line deformation	Loose coupling
Dietz, 2007[8]	HOST (Euler-Bernouilli non-linear beam finite elements)	FLOWer (RANS solver, structured Chimera grids)	Hermite polynomials	Fictive work method	Loose coupling
Ortun, 2008[35]	MSC.Marc (beam finite elements)	elsA (RANS solver, structured Chimera grids)	Quarter chord line deformation used for each section, interpolated from the structural model	Spring analogy or elastic analogy continuous applied to cells group with interpolation within each group	Strong coupling
Biedron, 2008[6]	CAMRAD-II (non-linear beam finite elements)	FUN3D (RANS solver, unstructured overset grids)	Spline interpolation from the quarter-chord line deformation	Linear elasticity approach	Loose coupling
Sitaraman, 2009[11]	DYMORE (non-linear beam finite elements)	UMTURNS (RANS solver, structured grids) with a wake model	Interpolation from the quarter-chord line deformation	Interpolation from the quarter-chord line deformation with a cosine decay function using the blade distance	Strong coupling
Thepvongs, 2009[17]	UM/NLABS (non-linear beam finite elements)	FUN3D (RANS solver, unstructured grids)	Multiquadric-Biharmonic	Spring analogy based method	Strong coupling
Yoon, 2010[14]	In-house (Hodges beam finite elements)	In-house (RANS solver, structured overset grids)	Delaunay graph technique	Delaunay graph technique	Loose coupling
Present work	NASTRAN (non-linear beam finite elements)	HMB (RANS solver, structured multiblock grids)	CVT	SAM and TFI	Loose coupling

In general, most model rotors are stiffer than full scale ones and therefore the influence of the structural deformation is small, this decreases the influence of the aeroelastic coupling and does not allow for a thorough assessment of the improvements offered by CFD/CSD coupling methods. On the other hand, full scale rotor experiments can only be trusted at low and medium thrust due to the high level of interaction between the wake and the measurement setup, as shown by Shinoda *et al*[21]. Nevertheless, an attempt to quantify the influence of the stiffness of model rotors on the hover loads is shown in the work of Beaumier *et al*[22]. Their predicted torsional deformation at the tip of the 7A rotor was rather limited with an amplitude of −0·5° compared

https://doi.org/10.1017/S0001924000007107 Published online by Cambridge University Press

to the amplitude of −2° obtained on a simulation of the full-scale Bo-105 rotor. In general, rotor performance in hover is measured during flight tests but again the structural deformation is not known. For these reasons, there is a need for suitable experimental data for flexible rotor blades in hover.

At the core of all coupling methods for aeroelastic rotor calculations, there is a grid deformation technique. It is the objective of this paper to develop a hybrid coupling method that can be used with multi-block structured grids and can account for the blade deformation and the consequent deformation of the CFD mesh. This is the primary objective of this work. The method will be demonstrated for several cases including forced blade deformations following structural modes or static blade deformation like those encountered in hover. The demonstration cases used for this paper include full-scale and model scale rotor blades.

We also re-visit the mesh deformation method and propose a hybrid technique that maintains high mesh quality and is compatible with multi-block structured grids. This is demonstrated for several rotors in hover with prescribed deformation, and for cases where the blade shape is itself computed.

2.0 NUMERICAL METHODS

2.1 Aerodynamic modelling

The helicopter multi-block (HMB) code, developed at Liverpool, is used for the present work. HMB solves the Navier-Stokes equations in integral form using the arbitrary Lagrangian Eulerian (ALE) formulation for time-dependent domains with moving boundaries:

$$\frac{d}{dt}\int_{V(t)} \vec{\mathbf{w}} dV + \int_{\partial V(t)} \left(\vec{F}_i(\vec{\mathbf{w}}) - \vec{F}_v(\vec{\mathbf{w}})\right) \vec{n} dS = \vec{S} \qquad \ldots (1)$$

where $V(t)$ is the time dependent control volume, $\partial V(t)$ its boundary, $\vec{\mathbf{w}}$ is the vector of conserved variables $[\rho, \rho u, \rho v, \rho w, \rho E]^T$. $\vec{F}_i$ and $\vec{F}_v$ are the inviscid and viscous fluxes, including the effects of the mesh movement. For hovering rotor simulations, the grid is not rotating. A source term $\vec{S} = [0, -\rho \vec{w} \times \vec{u}_h, 0]^T$ is however added to compensate for the inertial effects of the rotation along with a velocity assigned to grid nodes. $\vec{u}_h$ is the local velocity field in the rotor-fixed frame of reference.

The Navier-Stokes equation are discretised using a cell-centred finite volume approach on a multi-block grid, leading to the following equations:

$$\frac{\partial}{\partial t}(\mathbf{w}_{i,j,k} V_{i,j,k}) = -\mathbf{R}_{i,j,k}(\mathbf{w}_{i,j,k}) \qquad \ldots (2)$$

where $\mathbf{w}$ represents the cell variables and $\mathbf{R}$ the residuals. i, j and k are the cell indices and $V_{i,j,k}$ is the cell volume. Osher's[23] upwind scheme is used to discretise the convective terms and MUSCL variable interpolation is used to provide third order accuracy. Van Albada limiter is used to reduce the oscillations near steep gradients.

Temporal integration is performed using an implicit dual-time step method. The linearised system is solved using the generalised conjugate gradient method with a block incomplete lower-upper (BILU) preconditioner[24].

Multi-block structured meshes are used for HMB. These meshes are generated using ICEM-Hexa™ of ANSYS. The multi-block topology allows for an easy sharing of the calculation load

https://doi.org/10.1017/S0001924000007107 Published online by Cambridge University Press

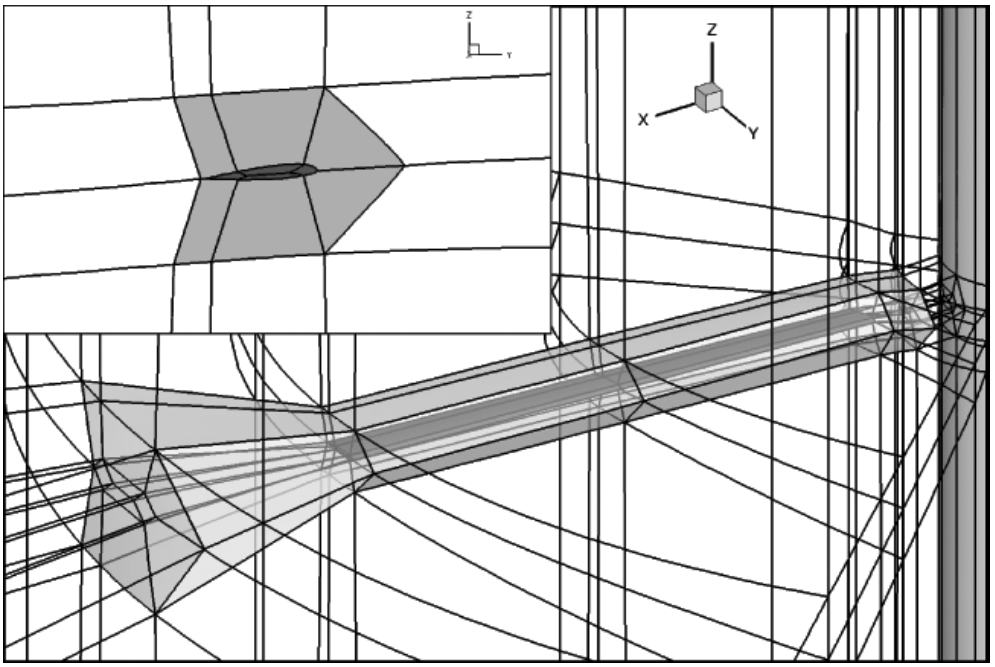


Figure 1. Multi-block grid topology used by HMB for hover cases, showing the blade (dark grey), the cylindrical hub (light grey) and the rigid blocks (translucent grey). A section perpendicular to the blade span at the tip is shown in the upper left corner.

for parallel computing. For rotor flows, a typical multi-block topology used in the University of Liverpool is described in Ref. 25. A *C*-mesh is used around the blade and this is included in a larger *H* structure which fills up the rest of the computational domain. The block boundaries for a hovering rotor blade are shown in black in Fig. 1. Rotor trimming, corresponding to rigid movements of the blade, is obtained by a rigid motion of the whole *C*-Part of the mesh, shown in grey in Fig. 1. This preserves the mesh quality around the blade surface. The layer of blocks around the *C*-part is then re-meshed using the trans-finite interpolation method[26].

2.2 Structural modelling

NASTRAN is used for calculating the static structural deformations of a blade that is modelled as a beam. Non-linear CBEAM elements are used along the quarter-chord line of the blade and contain all the blade structural properties. A non-linear static analysis is performed (SOL 106), taking into account the centrifugal forces. This is followed by an iterative process allowing for the large displacements to be taken into account while recomputing the forces due to the aerodynamic loads and the centrifugal forces at each step. The main structural properties needed for this analysis are the distributions of the sectional area, the chordwise and flapwise area moments of inertia, the torsional constant and the linear mass distribution along the span. The offset between the elastic axis and the centre of gravity along the span can also be added to refine the analysis. All structural properties are linearly interpolated between the ends of the beam element. CBAR elements without any structural properties are also used for interpolating the beam model deformation to the blade surface, which is then used for deforming the fluid grid.

https://doi.org/10.1017/S0001924000007107 Published online by Cambridge University Press

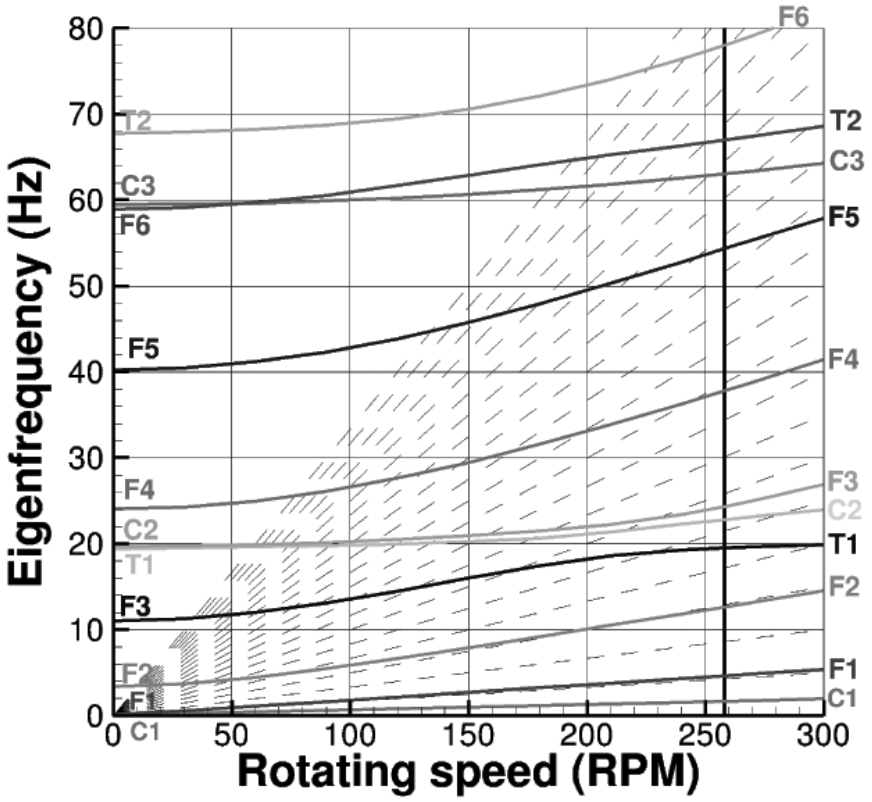


Figure 2. Evolution of the UH-60A blade eigenfrequencies with rotational speed.

The UH-60A[27] and HART-II[28] blades are used as examples. The UH-60A blade geometry has a rectangular planform shape until $r/R = 0{\cdot}93$ from where the tip is swept back by 20°. Two aerofoil sections are used, with linear transitions in between: the SC1095 from $r/R = 0{\cdot}1925$ to $r/R = 0{\cdot}4658$ and from $r/R = 0{\cdot}8540$ to the tip, and the SC1094R8 from $r/R = 0{\cdot}4969$ to $r/R = 0{\cdot}8230$. The blade has non-linear twist as reported in Ref. 27 In the literature, Ho *et al*[29] used a structural model that included some aspects of the hub as well as the elements of the blade. The approach used here is different, since a simplified hub model is used. The employed NASTRAN model contained 89 CBEAM elements along the blade span, and the blade properties reported by Hamade *et al*[30] were used. The blade model was attached to the hub at the radial station $r/R = 0{\cdot}093$ and was not allowed any translation at the root. The blade was free to flap and lead-lag but the root of the blade was not allowed to have any pitching motion. A lead-lag damper and a flapping spring were added as elastic elements with a strength of 353lbf.ft/rad. This simple hub model was deemed efficient enough to predict the blade loading and thus deformation. The loads on the hub as well as the dynamic response of the hub due to the blade motion were not the focus of this work, limiting the interest for a more complex hub geometry. Figure 2 shows the eigenfrequency of the obtained modes as a function of the rotational speed.

https://doi.org/10.1017/S0001924000007107 Published online by Cambridge University Press

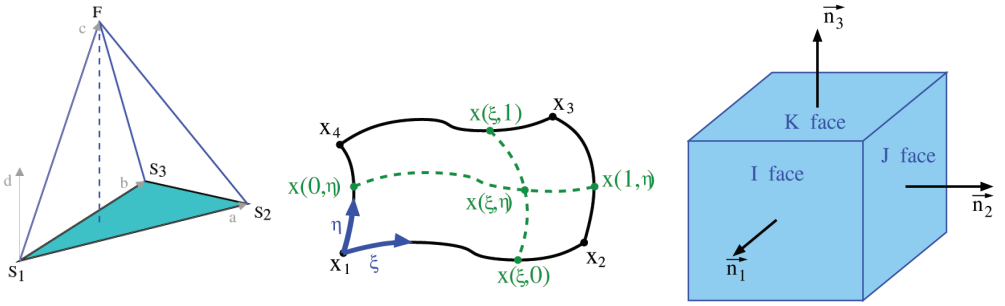


Figure 3. (a) Notations for the association of a fluid node F with a triangular element (S_1,S_2,S_3) using CVT. (b) Notation for the TFI application on a block face. (c) Notation for cell skewness definition.

The HART-II blade is of rectangular planform. A NACA23012 aerofoil with a 5mm tab is used along the blade span. The twist is linear, –8°/R. Its structural model contains 42 elements along the blade span. For CFD/CSD coupling, the aerodynamic loads are first extracted from the fluid solution and are then used in NASTRAN to obtain the required blade shape. The blade is then deformed based on the structural shape using the method described in the next section. This process is repeated until convergence.

2.3 Grid deformation method

The method developed for HMB first deforms the blade surface using the constant volume tetrahedron (CVT) method, then obtains the updated block vertex positions via spring analogy (SAM) and finally generates the full mesh via transfinite interpolation (TFI). This method uses the properties of multi-block meshes and maintains its efficiency as the number of blocks increases, particularly in the spanwise blade direction. This approach has not been reported elsewhere in the literature since most authors deform the complete mesh using the mode shapes. The proposed method provides more flexibility and allows for complex multi-block topologies to be used. In addition it gives more control over the distribution of mesh deformation in the computational domain.

Constant volume tetrahedron (CVT) method The constant volume tetrahedron (CVT) method[31] projects each fluid node to the nearest structural triangular element and moves it linearly with the element.

Each node of the blade surface (F) is associated with a structural element (S_1,S_2,S_3) and projected as follows:

$$\vec{c} = \alpha\vec{a} + \beta\vec{b} + \gamma\vec{d} \qquad \ldots (3)$$

where $\vec{a} = \overrightarrow{S_1S_2}$, $\vec{b} = \overrightarrow{S_1S_3}$, $\vec{c} = \overrightarrow{S_1F}$ and $\vec{d} = \vec{a}\Lambda\vec{b}$. The notation is also explained in Fig. 3(a). The coefficients α, β and γ can then be calculated using:

$$\beta = \frac{\left(\vec{b}\cdot\vec{c}\right)\|\vec{a}\|^2 - \left(\vec{a}\cdot\vec{b}\right)(\vec{a}\cdot\vec{c})}{\|\vec{a}\|^2\|\vec{b}\|^2 - \left(\vec{a}\cdot\vec{b}\right)^2} \qquad \ldots (4)$$

https://doi.org/10.1017/S0001924000007107 Published online by Cambridge University Press

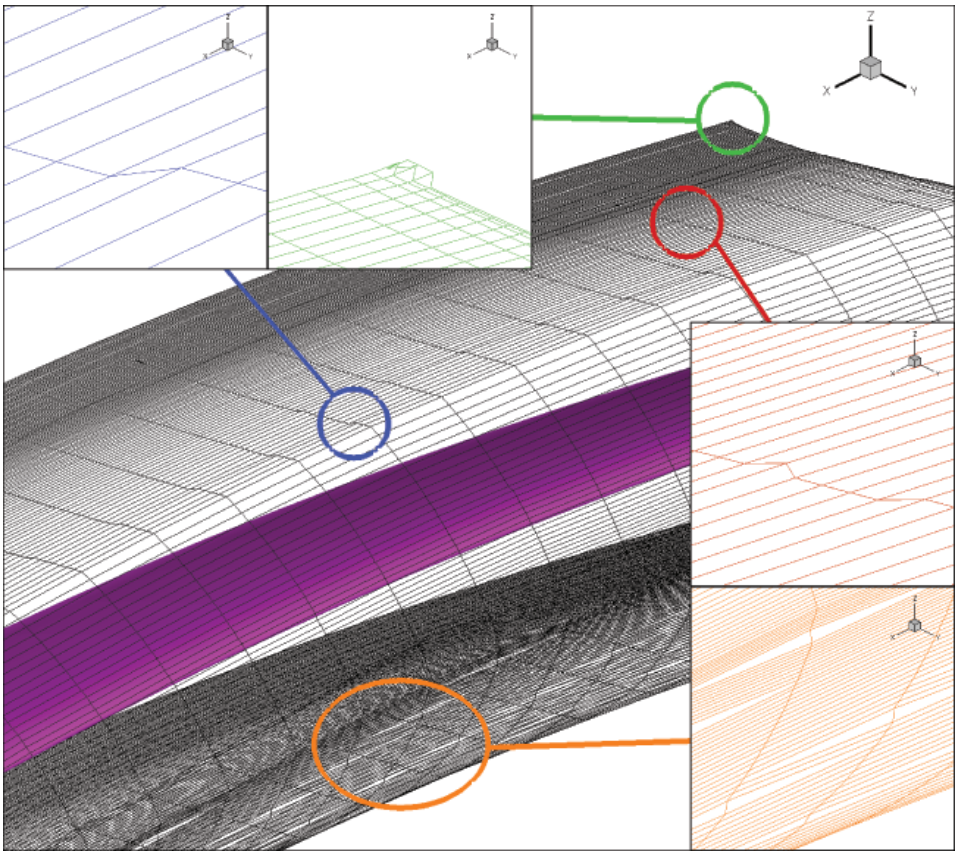


Figure 4. Distortion of the mesh due to the use of CVT far from the blade surface.

$$\beta = \frac{\left(\vec{b}\cdot\vec{c}\right)\|\vec{a}\|^2 - \left(\vec{a}\cdot\vec{b}\right)\left(\vec{a}\cdot\vec{c}\right)}{\|\vec{a}\|^2\|\vec{b}\|^2 - \left(\vec{a}\cdot\vec{b}\right)^2} \quad \ldots (5)$$

$$\gamma = \frac{\left(\vec{c}\cdot\vec{d}\right)}{\|\vec{a}\|^2\|\vec{b}\|^2 - \left(\vec{a}\cdot\vec{b}\right)^2}\cdot \quad \ldots (6)$$

The new position of the deformed blade fluid point is obtained by calculating:

$$\vec{c'} = \alpha\vec{a'} + \beta\vec{b'} + \gamma\vec{d'}\,, \quad \ldots (7)$$

where $\vec{a'}$, $\vec{b'}$, $\vec{c'}$ and $\vec{d'}$ are the same vectors after the structural deformation.

The CVT is an efficient deformation method, however, it showed limitations when used further from the blade, because the linear association with the triangular structural elements can create discrepancies between two close nodes associated with two different structural elements as shown in Fig. 4. Therefore, the mesh deformation further from the blade surface has to be performed with a different method. A transfinite interpolation (TFI) was therefore introduced in the *C*-part of the mesh.

https://doi.org/10.1017/S0001924000007107 Published online by Cambridge University Press

Trans-finite interpolation (TFI) The trans-finite interpolation (TFI), described by Dubuc *et al*[26], is used to interpolate the block face deformation from the edge deformations and then the full block deformation from the deformation of the block faces.

The mesh deformation uses a weighted approach to interpolate a face/block from the boundary vertices/-surfaces, respectively. The weight depends on the curvilinear co-ordinate divided by the length of the curve. The notation used here is shown in Fig. 3(b). The generation of the mesh on a block face ($\vec{x}_1, \vec{x}_2, \vec{x}_3, \vec{x}_4$) can be expressed as:

$$d\vec{x}(\xi,\eta) = \vec{f}_1(\xi,\eta) + \phi_1^0(\eta)[d\vec{x}_1(\xi) - \vec{f}_1(\xi,0)] + \phi_2^0(\eta)[d\vec{x}_3(\xi) - \vec{f}_1(\xi,1)]\,, \quad \ldots (8)$$

where $\vec{f}_1$ is defined as:

$$\vec{f}_1(\xi,\eta) = \psi_1^0(\xi)d\vec{x}_4(\eta) + \psi_2^0(\xi)d\vec{x}_2(\eta)\,, \quad \ldots (9)$$

with $d\vec{x}_1$, $d\vec{x}_2$, $d\vec{x}_3$ and $d\vec{x}_4$, , representing the displacements of the four vertices of the face and φ and ψ representing the blending functions in the η and ξ directions. The blending functions are expressed as functions of the stretching functions s_1, s_2, s_3 and s_4:

$$\psi_1^0(\eta) = 1 - s_1(\xi) \quad \ldots (10)$$

$$\psi_2^0(\eta) = s_3(\xi) \quad \ldots (11)$$

$$\phi_1^0(\eta) = 1 - s_4(\eta) \quad \ldots (12)$$

$$\phi_2^0(\eta) = s_2(\eta)\,, \quad \ldots (13)$$

and the stretching function s_1 is defined by:

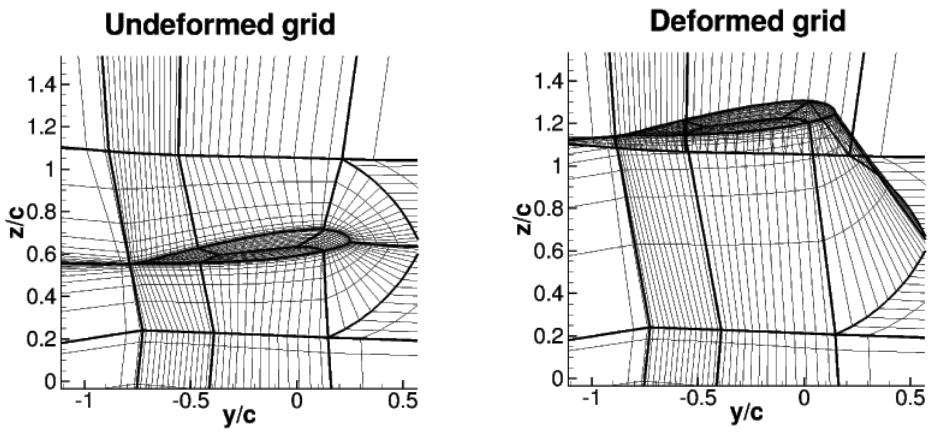
$$s_1(\xi) = \frac{x_1\widehat{x(\xi,0)}}{\widehat{x_1x_2}}\,, \quad \ldots (14)$$

where $\widehat{x_1x_2}$ is the curvilinear length between $\vec{x}_1$ and $\vec{x}_2$. s_2, s_3 and s_4 are defined in a similar way for the curves x_2x_3, x_3x_4 and x_4x_1 respectively. The interpolation inside the block from the shape of the block faces follows the same method.

This interpolation was introduced in the *C*-part of the mesh giving good results in terms of mesh quality but was limited in amplitude due to the small size of the *C*-part, as shown in Fig. 5. The block edges are not moved and therefore the maximum amplitude for each point has to be limited to a fraction of the *C*-part height, which often is about 0·2*c*. This limit in the displacement of the blade surface can easily be exceeded for rotor cases. To overcome this problem, the boundaries of the blocks around the blades are moved according to the blade deformation, and damping must be introduced when getting further from the blade to get no deformation at the calculation boundaries. Particular attention is paid to the mesh quality close to the blade as CFD calculations are sensitive to a loss of quality in the refined part near the blade surface.

Spring analogy (SAM) To overcome the problem demonstrated on Fig. 5, the spring analogy was used. The spring analogy[32] consists of adding springs on each block surface, side, and diagonal of the mesh. The springs along the sides of the surfaces tend to avoid large compression

https://doi.org/10.1017/S0001924000007107 Published online by Cambridge University Press



(a) Initial mesh (b) Deformed mesh

Figure 5. Limitations on the displacement amplitude due to the use of CVT and TFI. The blade tip was moved vertically with an amplitude of 0·6*c* outside the *C*-part of the mesh.

or dilatation of the block surfaces and the ones on the diagonals tend to limit skewness, which is critical in some parts of the mesh like the tip of the blade where the cells may be skewed.

The strength of the springs is set as the inverse of their length. The springs in contact with the blade are usually made stiffer (by a coefficient arbitrarily set to 50) to make the blocks close to the blade surface extremely rigid. An example of spring location and stiffness for a *C*-mesh around an aerofoil is shown in Fig. 6, where the springs on two faces are shown with black and dark grey dashed lines. The black lines represent the normal springs inside the computational domain and the dark grey ones are in contact with the blade and are therefore made stiffer. The force on each vertex is calculated as the sum of the forces due to the neighbouring springs:

$$\overrightarrow{F_i^v} = \sum_{j=1}^{n_i} k_{ij} \left(\overrightarrow{\delta_j} - \overrightarrow{\delta_i} \right) . \qquad \ldots (15)$$

n_i is the number of vertices connected to the *i*th vertex, k_{ij} is the stiffness of the spring between the *i*th and *j*th nodes and $\vec{\delta}_i$ is the displacement vector of the *i*th node.

The connection of the springs between the nodes, instead of the nodes and their original position is justified by the large displacements undergone by the blades and the need to keep the blocks close to the blade as close as possible to their undeformed shape.

The displacement of the nodes on the blade surface is forced by CVT, the nodes on the boundaries are kept at the same position, and SAM is applied to the vertices position to reach a new spring forces equilibrium This equilibrium is obtained by solving, for each node, the equation:

$$\sum_{j=1}^{n_i} \overrightarrow{F_{ij}^v} = \vec{0} , \qquad \ldots (16)$$

where $\overrightarrow{F_{ij}^v}$ is the force exerted on the *i*th node by the spring between the *i*th and *j*th nodes and is defined by $\overrightarrow{F_{ij}^v} = k_{ij}\,\vec{\delta}_j - \vec{\delta}_i$. Equation 16 can then be written as:

https://doi.org/10.1017/S0001924000007107 Published online by Cambridge University Press

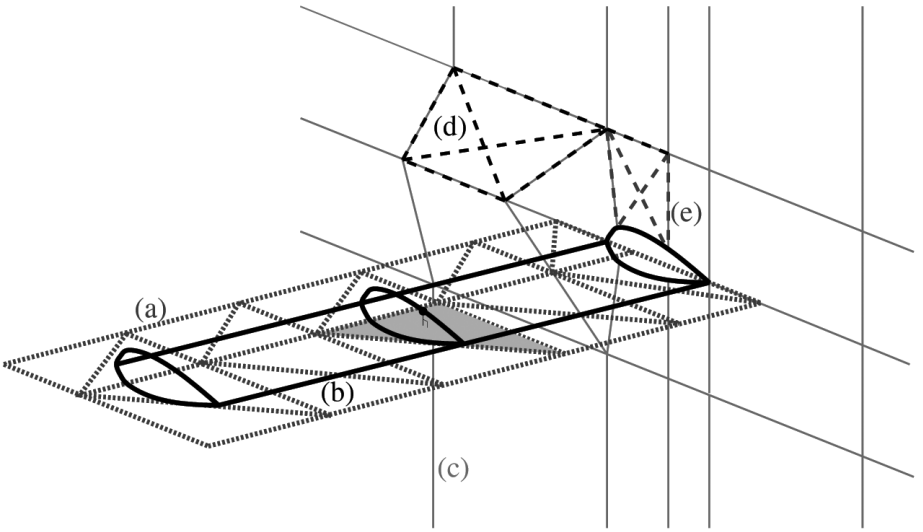


Figure 6. Projection of the fluid grid on the structural model through CVT. The blade structural model (a) is in grey short dashed line and the projection element in light grey. The blade shape (b) is represented in black. The fluid mesh block boundaries are shown in light grey (c), and the springs created for the spring analogy are shown in two block faces: in grey long dashed lines when in contact of the blade (e) and black long dashed lines otherwise (d).

$$\sum_{j=1}^{n_i} k_{ij} \left(\vec{\delta_j} - \vec{\delta_i} \right) = 0 \,. \qquad \ldots (17)$$

The above system of equations can also be written for each $\vec{\delta}_i$ as:

$$\vec{\delta_i} = \frac{\sum_{j=1}^{n_i} k_{ij} \vec{\delta_j}}{\sum_{j=1}^{n_i} k_{ij}} \qquad \ldots (18)$$

and solved iteratively, by using the algorithm:

$$\overrightarrow{\delta_{i,new}} = \frac{\sum_{j=1}^{n_i} k_{ij} \overrightarrow{\delta_{j,old}}}{\sum_{j=1}^{n_i} k_{ij}} \quad . \qquad \ldots (19)$$

This iterative process is initialised with the undeformed location of the nodes except for the ones on the blade surface which are set to the deformed position. The iterative process is repeated about 1, 000 times, which was enough to reach convergence even on meshes with a large number (more than 2,000) of vertices. The convergence criterion employed here was:

$$error = \sqrt{\sum_{i=1}^{n_v} \| \overrightarrow{\delta_{i,new}} - \overrightarrow{\delta_{i,old}} \|^2} \,. \qquad \ldots (20)$$

https://doi.org/10.1017/S0001924000007107 Published online by Cambridge University Press

2.4 Rotor trimmer

A simple grid trimmer based on the blade element theory described in Ref. 25 was used for this work. This model is based on the lock number γL of the blade and computes an initial trim state for a hovering rotor. Firstly, the collective is estimated as:

$$\theta_0 = \frac{3}{\sigma a_l} C_T + \frac{3}{2}\sqrt{\frac{C_T}{4}} \qquad \ldots (21)$$

where C_T is the thrust coefficient, a_l is the lift slope factor of the blade section, approximated by 5·7 for this work, and σ is the rotor solidity. The inflow factor λ is then estimated by:

$$\lambda = -\sqrt{\frac{C_T}{4}} = -\frac{\sigma a}{16}\left[\sqrt{1 + \frac{64}{3\sigma a}\theta_0} - 1\right] \quad . \qquad \ldots (22)$$

and the coning β_0 is:

$$\beta_0 = \frac{\gamma}{8}\left[\theta_0 + \frac{4}{3}\lambda\right] \qquad \ldots (23)$$

HMB is then used to compute the thrust coefficient $C_{T,CFD}$ at this particular trimming.

The next step uses the resulting thrust coefficient to update the trim state. The collective update ($\delta_{\theta 0}$) is calculated by:

$$\delta\theta_0 = \frac{C_{T,Target} - C_{T,CFD}}{\frac{dC_T}{d\theta_0}} \qquad \ldots (24)$$

with $\frac{dC_T}{d\theta_0}$ obtained by:

$$\frac{dC_T}{d\theta_0} = \frac{\sigma a}{6}\left[1 - \frac{1}{\sqrt{1 + \frac{64}{3\sigma a}\theta_0}}\right] \quad . \qquad \ldots (25)$$

The coning is then obtained using Equation 23, and the process is repeated until convergence.

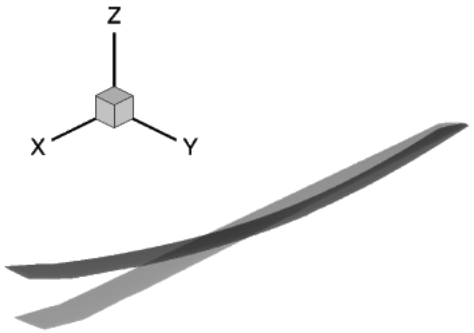
3.0 RESULTS AND DISCUSSION

3.1 Demonstration of the hybrid mesh deformation method

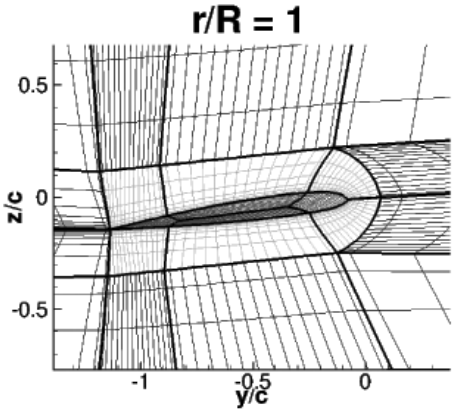
The proposed method was tested for the UH-60A rotor blade, using a relatively large deformation, typical of main rotors. The HART-II rotor experiment showed deformation reaching −0·4c to 0·2c in elastic flapping at the tip and −3·5 to 2° in elastic torsion at the tip[28]. The proposed method is demonstrated here for higher deformation levels in order to prove its ability to deal with all expected cases. Although the UH-60A blades in-flight deformation is not known, the measurements of the HART-II rotor provide some insight in the expected deformation amplitudes.

The resulting grid quality was assessed using two criteria: the volume ratio $(\frac{V_{new}}{V_{old}})$ and the

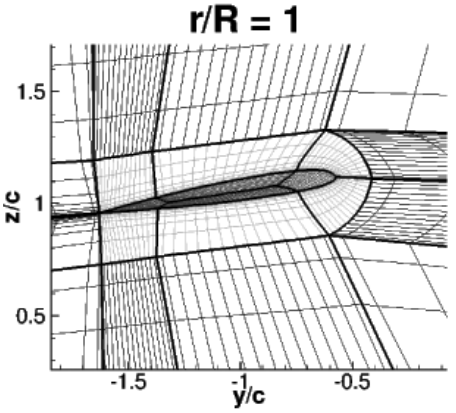
https://doi.org/10.1017/S0001924000007107 Published online by Cambridge University Press



(a) Shape comparison



(b) Undeformed blade, section of the mesh at the tip



(c) Deformed blade, section of the mesh at the tip

Figure 7. Deformation of the UH-60A blade using the second flapping mode with 0·5*c* of tip amplitude and the first torsional mode with −9° of tip amplitude. A collective angle of 5° and a coning angle of 2° were also added. Mesh on the blade is dark grey, mesh in the stiffer blocks is light grey. The block boundaries are shown as thick black lines (every third mesh line shown).

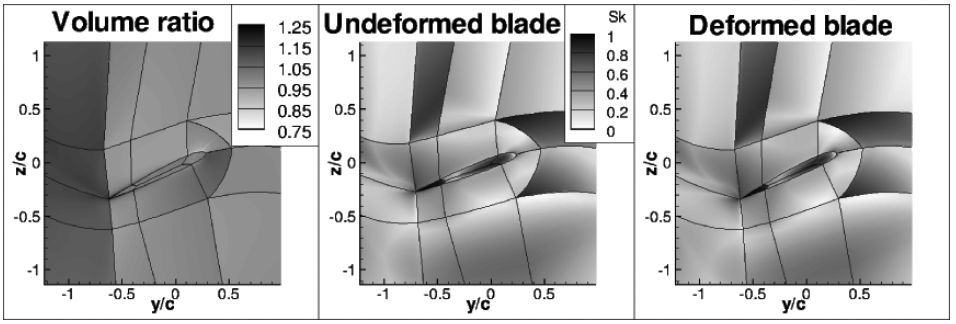
cell skewness change. The cell skewness *Sk* is computed as:

$$Sk = \max\,(n_i.n_j),\ i \neq j \qquad \ldots\ (26)$$

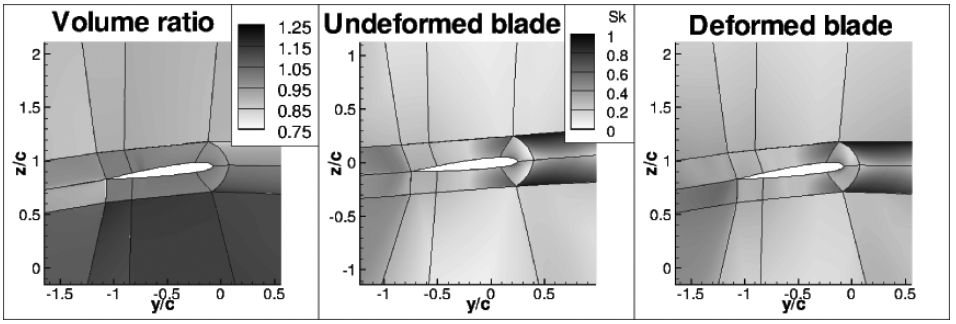
where $\vec{n}_i$ is the unit normal vector on the *i*th face following the notations of Fig. 3(c).

The method was tested by coupling the blade rigid motion with structural deformations following eigenmode shapes obtained through a modal analysis performed with NASTRAN. The rigid motion consisted of an increase of the collective angle by 5° and of the coning angle by 2°. The blade was also deformed following the second flapping mode with an amplitude of 0·5*c* upwards at the tip and the first torsional mode with an amplitude of 9° at the tip, pitching downward. The mesh qualities at a section near the root of the blade, a section at the beginning of the swept back tip, and a section at the tip were assessed. Visualisation of the blade shape, and a comparison of a mesh section before and after deformation are shown in Fig. 7. Despite the strong deformation, the changes in mesh quality were limited, particularly close to the blade.

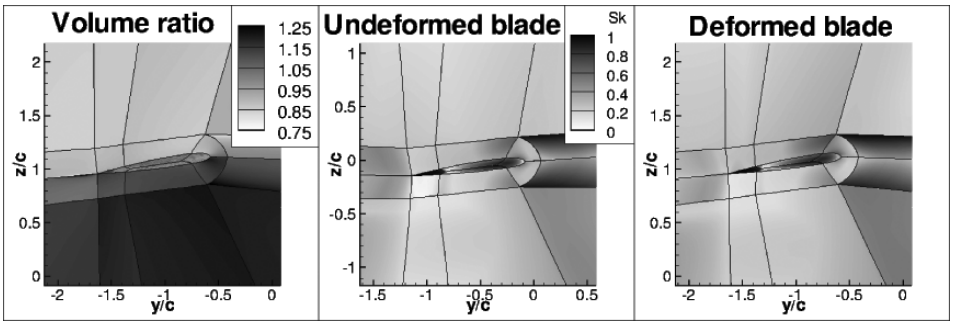
https://doi.org/10.1017/S0001924000007107 Published online by Cambridge University Press



(a) Root area



(b) Start of the sweep back



(c) Tip of the blade

Figure 8. Comparison of the cell volume and skewness in planes perpendicular to the blade before and after a deformation following the second flapping mode with an amplitude of 0·5*c* at the tip, and the first torsional mode with an amplitude of −9°. A coning angle of 2° as well as a collective angle of 5° were added to the deformations.

This is shown in Fig. 8 using the mesh quality criteria. Due to the high level of deformation at the tip, the spring analogy resulted in large volume changes in the *C*-part of the mesh. However, due to the small changes in cell skewness, the mesh quality was still acceptable. This result also serves to demonstrate the flexibility of the mesh deformation method for a complex mesh topology.

https://doi.org/10.1017/S0001924000007107 Published online by Cambridge University Press

Table 2
Evolution of the grid quality with the increase of the blade deflection

Tip deflection	Volume ratio min (near blade)	Volume ratio max (near blade)	Skr_{max} (near blade)	Volume ratio min (full grid)	Volume ratio max (full grid)
0·3*c*	0·8555	1·1423	0·9856	0·8555	1·1939
0·6*c*	0·7494	1·2654	0·9724	0·7494	1·3879
0·9*c*	0·6250	1·3343	0·9688	0·6250	1·5820
1·2*c*	0·5000	1·4322	0·9616	0·5000	1.7762
1·5*c*	0·3745	1·5437	0·9652	0·3745	1·9705
1·8*c*	0·2489	1·6572	0·9292	0·2489	2·1649
2·1*c*	0·1237	1·7724	0·9232	0·1237	2·3595

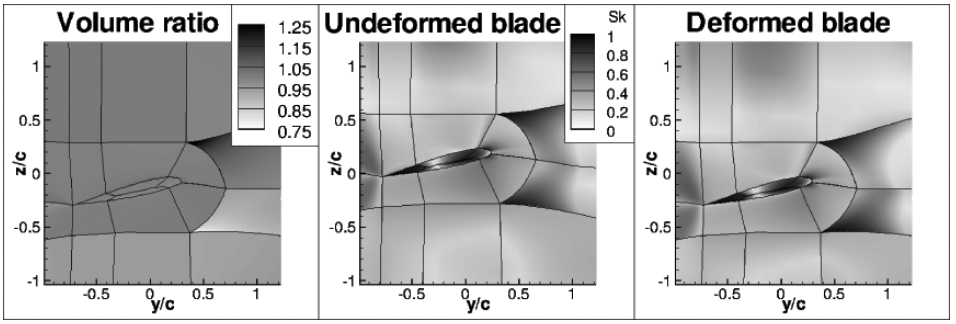
The grid quality was also tested for deformations following the second flapping mode with various tip deflection amplitudes. The results are presented in Table 2. The maximum skewness in the blocks near the blade is limited as shown by the max skewness ratio Skr_{max}. The volume ratio was then used to determine the maximum acceptable deformation. In order to preserve the grid properties (e.g. wall spacings for the boundary layer), the volume ratio was better kept between 0·5 and 2. The requested deformation amplitude was limited to 1·2*c*. The location of the largest cell volume change is around the main part of the blade which was allocated to in a single block in the span-wise direction. If this block was divided in two, the spring analogy would move the block boundaries according to the blade movements and would improve further the grid quality.

3.2 HART-II rotor in hover

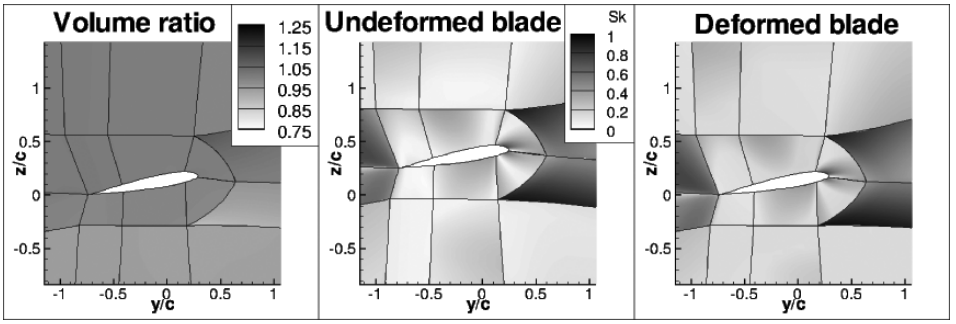
An assessment of the mesh deformation method was also carried out for the HART-II rotor, using calculations with increasing blade bending deformations. A first calculation used the undeformed blade, while a second and a third computed a blade deformed according to the second flapping mode. The amplitudes of the deformations were set to 0·3*c* and 0·6*c* at the tip, and termed half-deformed and deformed blades, respectively. In practice, it is unlikely that a blade in hover will be deformed according to the second flapping mode at such high amplitudes. Nevertheless, the test was quite difficult and used to assess the proposed method for complex mode shape deformations. The HART-II experiment measured flapping deflections up to 0·3*c* and torsional deformations up to 2° at the tip. The selected higher deformation level aimed at demonstrating the method ability to easily cope with such deformations. The conditions for the calculation were: tip Mach number 0·641 and tip Reynolds number $2{\cdot}659 \times 10^6$. The coning angle was set to $\beta_0 = 2{\cdot}2°$. Two values for the collective were tested: $\theta_0 = 8°$ and $\theta_0 = 12{\cdot}5°$. The grid quality for the largest deformation at three sections of the blade (root, middle and tip) is shown in Fig. 9. The cell volume changes were kept out of the *C*-part of the mesh, and the cell skewness was kept close to the original.

For $\theta_0 = 8°$, the surface pressure coefficient on the deformed blade is shown in Fig. 10(a). The deformation resulted in higher suction at the tip. After switching from an absolute frame of reference to a relative one, streamlines were generated near the blade surface to identify the topology of the flow. At the root of the blade, the effect of the root vortex appears to be similar for all cases. The effect of these vortices seems to be concentrated close the the root and the tip of the blade and does not have any substantial influence elsewhere. The flow is attached on the whole blade.

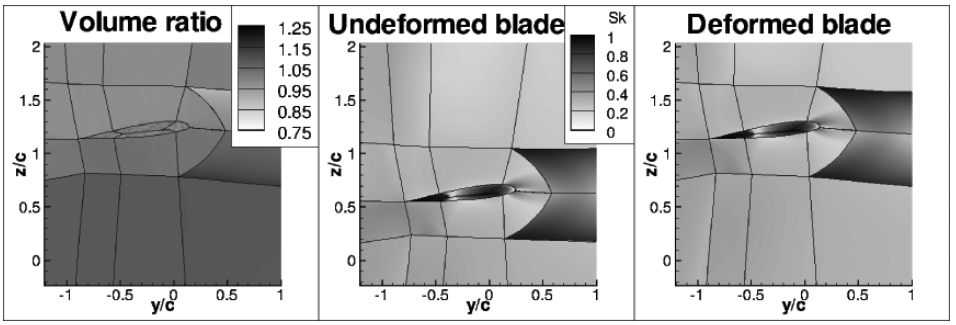
https://doi.org/10.1017/S0001924000007107 Published online by Cambridge University Press



(a) Root of the blade



(b) Middle of the blade

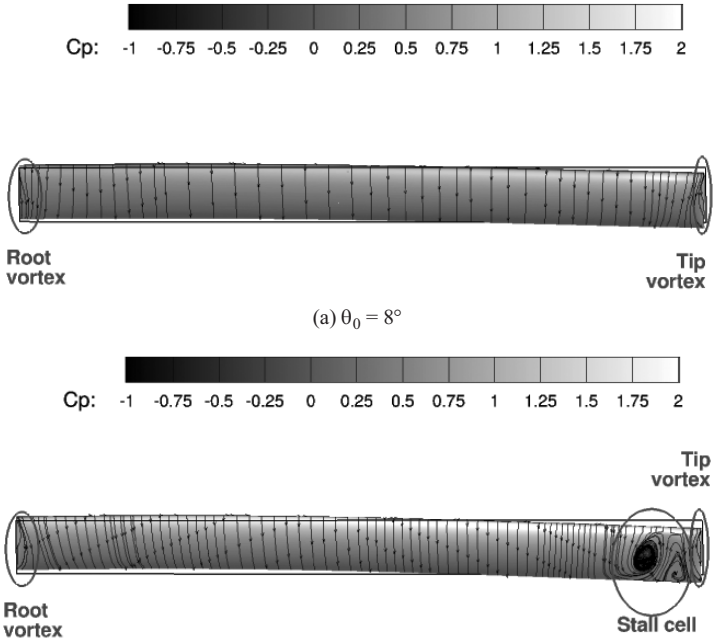


(c) Tip of the blade

Figure 9. HART-II rotor deformation following the second flapping mode with an amplitude of 0·6*c* at the tip. The first column shows the comparison of the cell volume ratio. The second and third columns show the skewness (*Sk*) of the undeformed and deformed grids. Three sections along the blade are shown: (a) root of the blade, (b) mid-span and (c) blade tip.

The increase in loading due to the higher suction at the tip is also visible in Fig. 11(b) which shows the distribution of the sectional force loading S_F along the span. Apart from the loading, the blade twist as extracted from the deformed mesh is represented along with the geometric deflection of the blade. The results are consistent with the decrease of blade twist linked with the structural deformations. The effect of blade deformation is the opposite of what one would expect since Yoon *et al*[14] suggest a reduction in loading for the elastic blade with respect to the

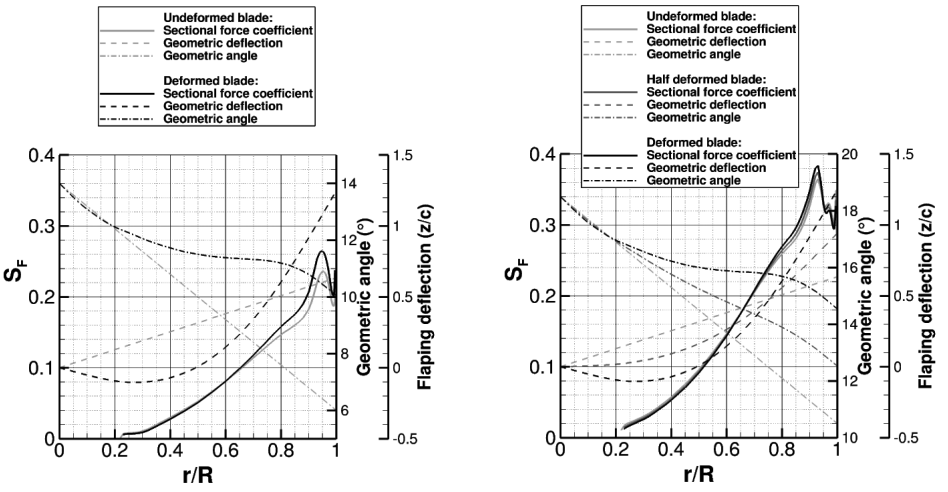
https://doi.org/10.1017/S0001924000007107 Published online by Cambridge University Press



(a) $\theta_0 = 8°$

(b) $\theta_0 = 12{\cdot}5°$

Figure 10. Pressure coefficient repartition on the upper surface of the deformed HART-II blade at collective 12·5°, with the outline of the undeformed blade.



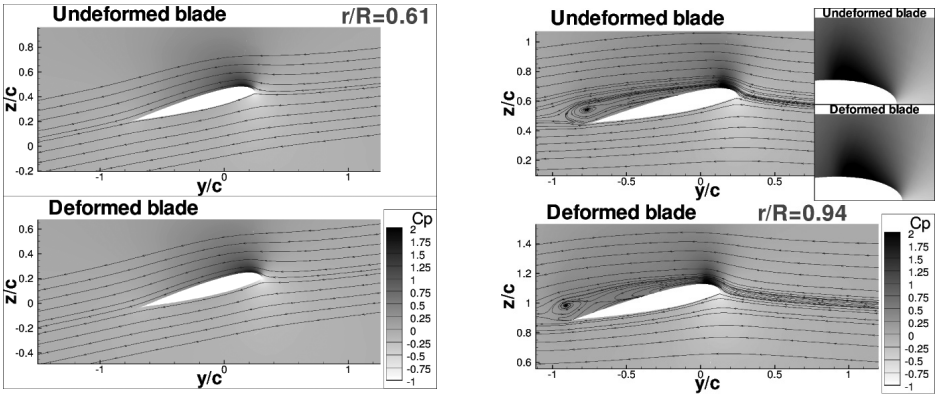
(a) $\theta_0 = 8°$

(b) $\theta_0 = 12{\cdot}5°$

Figure 11. Comparison of the sectional force coefficient SF along the blade span at collective 12·5°.

rigid one. However, the applied deformation follows the second flapping mode which is coupled with a torsional mode resulting in less twist near the tip as shown by the geometrical angle in Fig. 11(b), as obtained by adding the blade twist to the collective and the torsional deformation from the NASTRAN output. Consequently, the loads were higher for the deformed

https://doi.org/10.1017/S0001924000007107 Published online by Cambridge University Press



(a) $r/R = 0{\cdot}61$ (b) $r/R = 0{\cdot}94$

Figure 12. Comparison of the flow field at two blade sections at $r/R = 0{\cdot}61$ and $r/R = 0{\cdot}94$ for the undeformed and deformed blades.

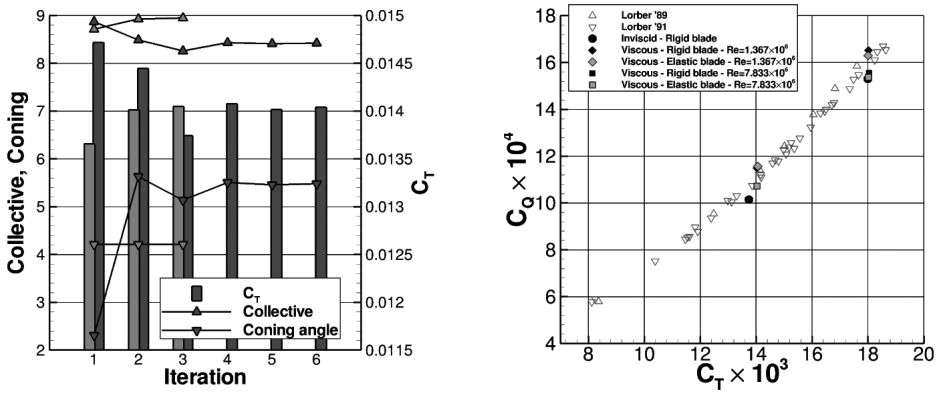
blade. Overall, up to 3° of difference in twist can be seen between the undeformed and the deformed blades with a maximum tip deflection.

The second case studied was at collective $\theta_0 = 12{\cdot}5°$. Figure 10(b) shows, for the deformed blade, the pressure coefficient distribution. Stalled conditions were selected so that the quality of the deformed mesh has a stronger influence on the solution. In general, to resolve the velocity and pressure gradients encountered in flow recirculation regions , a higher quality mesh is needed. Again, an increase of the loading at the tip due to the deformation appeared. Looking at the streamlines, the flow is attached on most of the blade, however, a stall cell appears over the last 10% of the blade. At the tip of the blade, the foot print of the tip vortex can also be seen. The tip stall cell is larger in the deformed blade case. The stall, however, is not caused by the deformation but it is due to the high collective of 12·5°. The above is shown in Fig. 11(b), where the span-wise sectional force coefficient S_F is computed along the blade. The tip is clearly stalled as suggested by the peak near 85%. Inboard of this peak, the effect of the deformation is more pronounced: the upward bending tip increases the blade loading over the undeformed value. Amongst the three configurations, the undeformed blade is less loaded near the tip and appears to have slightly higher loading inboards as can be seen for r/R between 0·2 and 0·5. The equivalent twist suggests that the deformed blade maintains a relatively low twist between $r/R = 0{\cdot}6$ and $r/R = 0{\cdot}85$. In the other two cases, the twist is more linear, which offloads the tip further. The loading increase at the tip due to the blade deformation was less pronounced than for the attached flow case.

Extracting the sectional flow field at two sections over the blade at $r/R = 0{\cdot}64$ and $r/R = 0{\cdot}94$ and converting the velocities from an absolute to a relative frame of reference as shown in Fig. 12, one can see attached flow at $r/R = 0{\cdot}64$ and separated flow at $r/R = 0{\cdot}94$. The shape of the streamlines and the isobars suggest that the loading is similar for both cases. This is not the case further outboards where the stall is fully developed. The 3D pattern of the stall is evident from the streamlines and one can notice the larger extent of the stalled area on the deformed blade. Again, the same range of pressure contours is used and the deformed blade appears to be more loaded.

The HART-II rotor was never tested in hover flight, therefore it is difficult to establish the stall boundary for the blade in hover flight. On the other hand, the obtained results appear reasonable. A second test-case with available experimental data was therefore used to assess the coupling strategy and the change in the flow characteristics due to the structural deformations.

https://doi.org/10.1017/S0001924000007107 Published online by Cambridge University Press



(a) (b)

Figure 13. (a) Trimming convergence history of the UH-60A rigid (dark grey) and elastic (third iteration, light grey) blades in hover during viscous calculations at $Re_{tip} = 1{\cdot}367 \times 10^6$. (b) Comparison of the thrust and torque coefficients (*CT* and *CQ* respectively) with experimental measurements from Lorber *et al* [18, 19].

3.3 Aeroelastic UH-60A rotor in hover

The selected test case to assess the influence of the aeroelastic coupling on the rotor performance is the UH-60A rotor. Wind-tunnel measurements were obtained by Lorber *et al*[18,19] for a thrust coefficient of $C_T/\sigma = 0{\cdot}17$ on a model rotor. This corresponds to $C_T = 0{\cdot}01404$. The UH-60A rotor was Mach-scaled with a diameter 5.73 times smaller than the real rotor and some blade deformation was included to reflect the structural deformations undergone by the blade in flight. The exact geometry of the scaled-model blade along with its structural properties were not available. It was therefore decided to compare the experimental results with a numerical simulation of the full scale rotor at the same thrust coefficient. The flight conditions then were: tip Mach number of 0·63, and Reynolds number based on the tip speed and chord length of $7{\cdot}833\times10^6$. It was also decided to use the experimental Reynolds number $Re_{tip} = 1{\cdot}367\times10^6$ for comparison, since viscosity could have a stronger effect on the torque. The experimental measurements provide integrated values like thrust and torque coefficients, and figure of merit. In addition, pressure taps along the blade span at eight radial stations and the position of the vortices in the wake were also measured. The pressure taps were located at $r/T = 0{\cdot}4$, 0·55, 0·675, 0·775, 0·865, 0·92, 0·945 and 0·965.

The first calculation was done for an inviscid flow with a small grid (1·5m nodes), while the following ones were on a larger grid (9m nodes) with a viscous flow model and the k–ω BSL turbulence model[33]. The viscous calculation was first run for a rigid blade at each Reynolds number, and then structural deformations were introduced. Each calculation was trimmed to the experimental thrust coefficient, using the method presented in Paragraph 2.4. To obtain the coning angle from the trimmer, a lock number of 8 was used for the full- and model-scale blades[34]. The structural model was based on the properties reported in Ref. 30 due to the lack of properties for the scaled-model. An example of rotor trimming is presented in Fig. 13(a), where the trimming of the rigid and elastic UH-60A blades with the viscous flow model is presented. A converged trim state was obtained after seven iterations for the rigid case and three for the elastic case, due to a better assessment of the initial collective thanks to the use of the trim state from the previous CFD/CSD coupling iteration.

https://doi.org/10.1017/S0001924000007107 Published online by Cambridge University Press

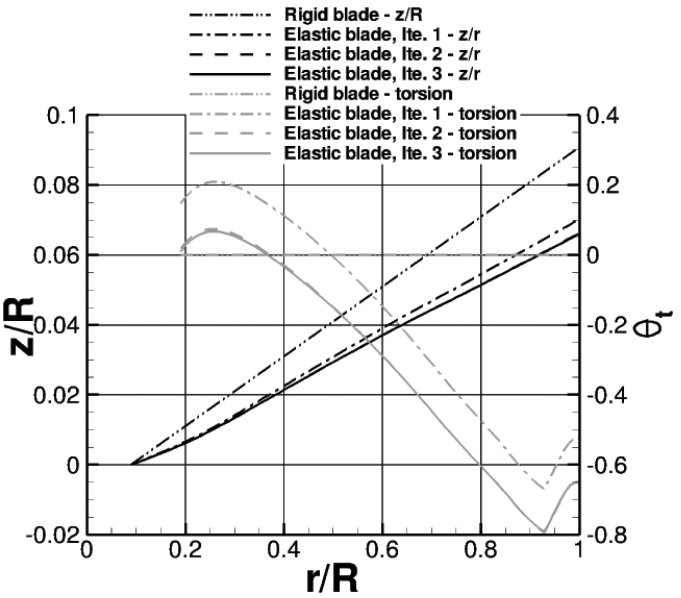


Figure 14. UH-60A blade deformation obtained from viscous calculations at $C_T/\sigma = 0{\cdot}170$ at $Re_{tip} = 1{\cdot}367 \times 10^6$.

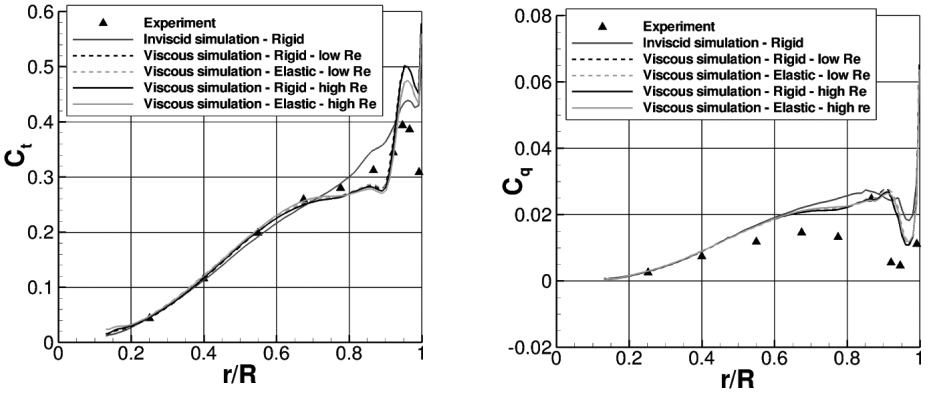
Table 3
Trim state and integrated coefficients for the various UH-60A calculations

Case	Reynolds number	θ_0	β_0	C_T	C_{QP}	C_Q	FM
InviscidcRigid blade	—	8·07	4·74	0·01374	0·001015	0·001015	0·7936
Viscous – Rigid blade	$1{\cdot}367 \times 10^6$	8·42	5·48	0·01403	0·001017	0·001083	0·7231
Viscous – Elastic blade	$1{\cdot}367 \times 10^6$	8·94	4·21	0·01406	0·001023	0·001157	0·7206
Viscous – Rigid blade	$7{\cdot}833 \times 10^6$	8·23	5·07	0·01402	0·000982	0·001070	0·7758
Viscous – Elastic blade	$7{\cdot}833 \times 10^6$	8·71	4·21	0·01403	0·000983	0·001072	0·7746

The structural deformations were recomputed after each CFD simulation, and the convergence of the blade loads was quick, within three iterations. The main differences between the inviscid and the viscous simulations are near the tip area, between $r/R = 0{\cdot}70$ and $r/R = 1$. This is mainly due to the coarseness of the inviscid grid compared to the viscous with the flow features in the area near the sweep tip not captured well by the inviscid model. The loading of the elastic blade is slightly stronger in the main part of the blade than the loading of the rigid blade, while it is lower closer to the tip. The blade deformations at $Re_{tip} = 1{\cdot}367 \times 10^6$ are shown in Fig. 14. The observed torsional effect for this coupled analysis has the opposite effect on loads compared to what happened for the HART-II blade where a second flapping mode deformation was prescribed.

The loading is consistent with the torsion added to the blade due to the structural deformations, with the tip undergoing a torsion up to −0·8° downwards. The trim state of each simulation is described in Table 3. The collective had to be increased by 0·5° for the deformed cases compared to the rigid to compensate for the blade torsion. The coning was also higher for the

https://doi.org/10.1017/S0001924000007107 Published online by Cambridge University Press



(a) Sectional thrust coefficient (b) Sectional torque coefficient

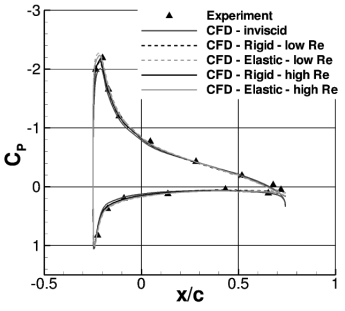
Figure 15. Comparison of the computed sectional thrust and moment coefficients (C_t and C_q respectively)along the rotor radius with the experiments from Lorber *et al*[18,19].

rigid blade simulations. The relatively high coning angle for the rigid blade may be due to the simple trimming method and lock number used here. The obtained torque coefficients are compared to experimental measurements[18,19] in Fig. 13(b) and show good agreement. The predicted torque values for deformed and undeformed blades are very close at $C_T = 0{\cdot}01404$ and these are mainly influenced by the Reynolds number. However, at higher thrust, the effect of the blade deformation tends to be more important even though not as important as the viscosity. The required torque coefficient was lower for the elastic blade, unlike the lower thrust case.

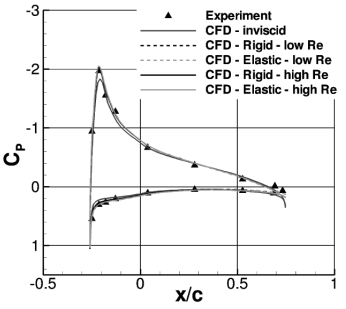
A more detailed comparison of the flow predictions with the experiments was carried out for $C_T = 0{\cdot}01404$. The distribution of the sectional thrust and moment coefficients is compared with the experimental results of Lorber *et al*[18,19] in Fig. 15. On the main part of the blade, the sectional thrust is very close to the experiment, however the peak at the tip is over predicted. This poor prediction may be due to approximations on the blade shape, due to uncertainties in its definition, or the location of the preceeding blade tip vortex, which comes extremely close to the blade at about $r/R = 0{\cdot}92$. The sectional torque is mainly over predicted, up to twice the experimental values in the main part of the blade. However the experimental coefficients were obtained by integrating the pressure on a limited number of taps at each section and this has a strong influence on the final figures. A further study by Schmitz *et al*[13] showed the effect of taking into account only the pressure at the tap locations and showed that the moment coefficient could be overestimated by more than 50% in the tip area. The influence of the Reynolds number showed little effect, mainly at about $r/R = 0{\cdot}90$ where the sectional lift and moment coefficient were slightly increased.

The pressure coefficients along the blade are plotted against the chord position in Fig. 16. The blade deformation increased the suction on the main part of the blade, but decreased it close to the tip, which is consistent with the torsional deformation undergone by the blade. The pressure coefficients from the simulations show good agreement with the experimental measurements up to the station at $r/R = 0{\cdot}675$. The higher suction peak predicted on the elastic blade was closer to the experiment, particularly at $r/R = 0{\cdot}40$. However, between $r/R = 0{\cdot}775$ and $r/R = 0{\cdot}92$, the suction peaks were under predicted and the pressure side showed a lower C_P . This explains the lower load in this part of the blade on the thrust distribution of Fig. 15(a). After $r/R = 0{\cdot}945$, the suction on the upper surface is over predicted, explaining the higher predictions of the

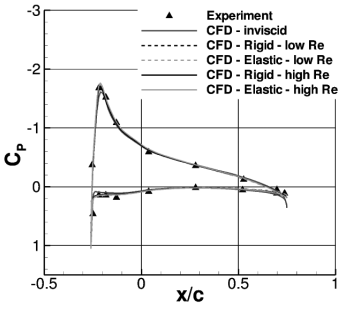
https://doi.org/10.1017/S0001924000007107 Published online by Cambridge University Press



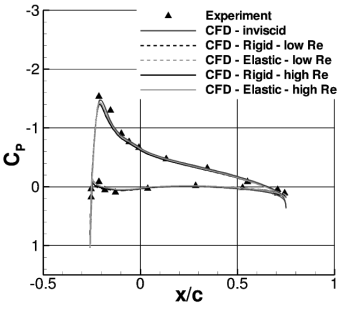
(a) $r/R = 0{\cdot}40$



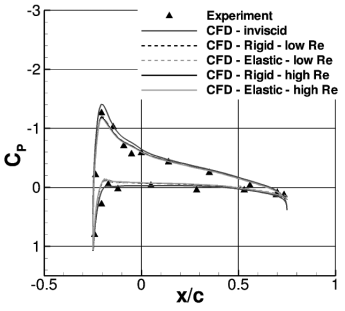
(b) $r/R = 0{\cdot}55$



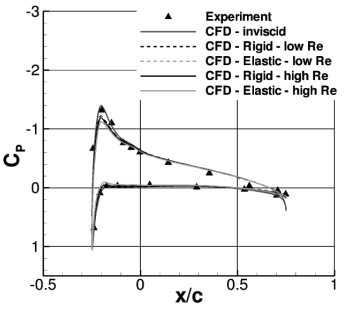
(c) $r/R = 0{\cdot}675$



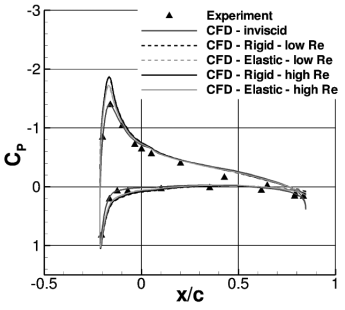
(d) $r/R = 0{\cdot}775$



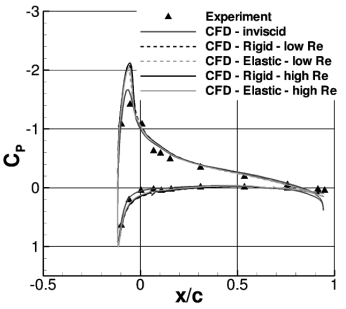
(e) $r/R = 0{\cdot}865$



(f) $r/R = 0{\cdot}92$



(g) $r/R = 0{\cdot}945$



(h) $r/R = 0{\cdot}965$

Figure 16. Comparison of the sectional pressure coefficients at various blade radial positions obtained with a rigid and elastic blade simulation with experimental measurements for hovering model (low Re) and full-scale (high Re) UH-60A rotors at $C_T/\sigma = 0{\cdot}170$. Experiments by Lorber *et al*[18].

https://doi.org/10.1017/S0001924000007107 Published online by Cambridge University Press

sectional thrust coefficient in the tip area in Fig. 15(a). These results could be due to a poor interpretation of the local twist of the original blade, or the position of the vortex from the preceeding blade, as previously explained. The predicted pressure coefficients show an equivalent angle-of-attack lower than the experimental predictions at the section $r/R = 0{\cdot}865$ and higher at the sections $r/R = 0{\cdot}945$ and $r/R = 0{\cdot}965$. This is consistent with the vortex effect around $r/R = 0{\cdot}92$ increasing the downwash at sections before $r/R = 0{\cdot}92$ and decreasing it at sections after $r/R = 0{\cdot}92$. The effect of the Reynolds number was limited on the pressure coefficients. When the pressure coefficients are projected along the thickness of the aerofoil, as shown in Fig. 17, the differences between the simulation and experimental results appear clearer. This projection shows the effect of the pressure coefficient on the sectional torque of the rotor, and therefore the bigger the differences, the worse the prediction of the rotor torque. Due to the few measurement locations on the sections, some important features are not well captured, like the stagnation point. This lack of resolution can explain the important differences between the predicted and experimental sectional torque seen in Fig. 15(b).

The vortex core location in the wake of the rotor has also been measured and compared to experimental results in Fig. 18. The effect of the Reynolds number on the vortex trajectories was marginal. The vortex vertical displacement is well predicted, while in the horizontal plane, the vortices tend to come slightly too fast inboard. Furthermore, after 270°, the grid cells become too coarse to accurately predict the location of the vortex cores and this explains the lack of agreement at the higher azimuth angles.

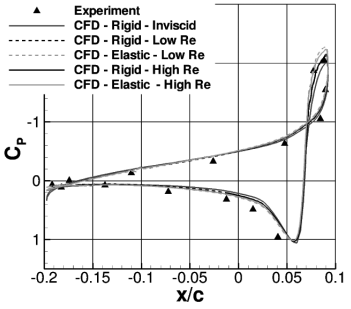
Overall, the flow predictions showed good agreement with the experimental data on the main part of the blade. The results, however, showed discrepancies with experiments near the tip. These could be due to uncertainties in the blade definition or the influence of the preceeding blade vortex. The lack of structural data for the model blade or the unknown blade shape during the experiment did not allow for a further investigation of this problem. The mesh deformation and trimming methods were found to be robust. While the mesh deformation did not result in any significant CPU overhead, the use of the grid trimmer increased the CPU cost by 50 to 100%, and a full coupled simulation needed twice the time of a rigid one.

4.0 CONCLUSIONS

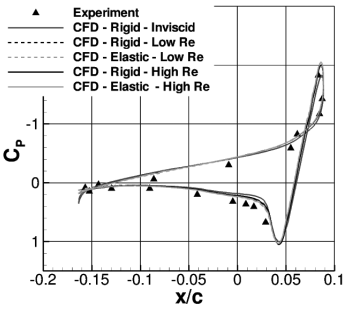
A CFD/CSD coupling method for the aeroelastic analysis of rotors in hover has been presented and demonstrated. This hybrid mesh deformation technique uses the constant volume tetrahedron method on the blade surface, spring analogy on the block edges and trans-finite interpolation inside blocks. The method is more general than a simple modal mesh deformation and proved to be robust and efficient. A first demonstration was performed for the HART-II rotor in hover, showing the ability of the method to handle blade deformations, though no experiments were available for comparison.

The demonstration was taken further by simulating the UH-60A rotor in hover using a coupled CFD/CSD procedure. However, the available experimental data did not allow for a complete validation of the simulation. Therefore, the properties of the full-scale rotor structural had to be used in order to assess the blade deformations even if the model rotor did not have the same behaviour as the full size blade. The comparison with the experiment showed a fairly good agreement for the blade loads and wake position. For all cases, the quality of the mesh was preserved. This was monitored using the relative volume changes of the cells as well as their skewness. The method had minimal overhead in terms of CPU time, and for a typical mesh of 9m points per blade, fewer than 15 CPU seconds were necessary for the deformation and re-meshing.

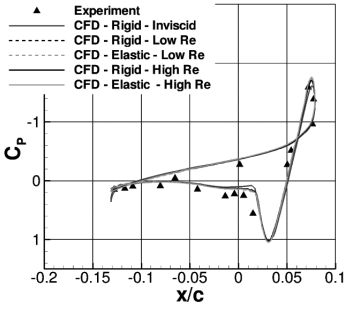
https://doi.org/10.1017/S0001924000007107 Published online by Cambridge University Press



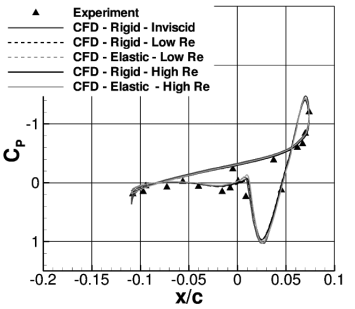
(a) $r/R = 0{\cdot}40$



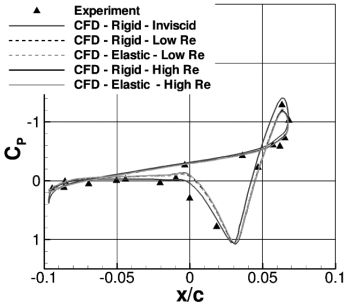
(b) $r/R = 0{\cdot}55$



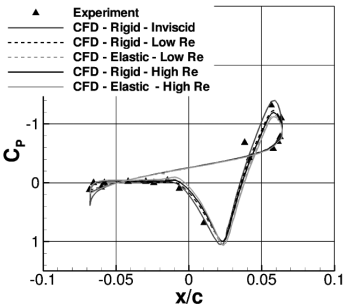
(c) $r/R = 0{\cdot}675$



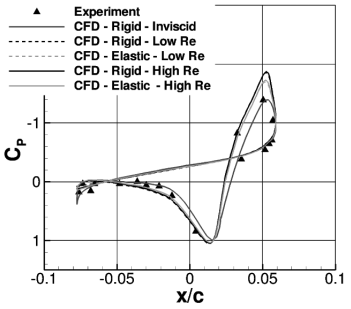
(d) $r/R = 0{\cdot}775$



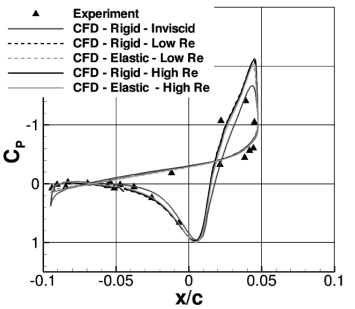
(e) $r/R = 0{\cdot}865$



(f) $r/R = 0{\cdot}92$



(g) $r/R = 0{\cdot}945$



(h) $r/R = 0{\cdot}965$

Figure 17. Comparison of the sectional pressure coefficients at various blade radial positions obtained with a rigid and elastic blade simulation with experimental measurements for hovering model (low Re) and full-scale (high Re) UH-60A rotors at $C_T/\sigma = 0{\cdot}170$. The pressure coefficients are projected on the aerofoil thickness. Experiments by Lorber *et al*[18].

https://doi.org/10.1017/S0001924000007107 Published online by Cambridge University Press

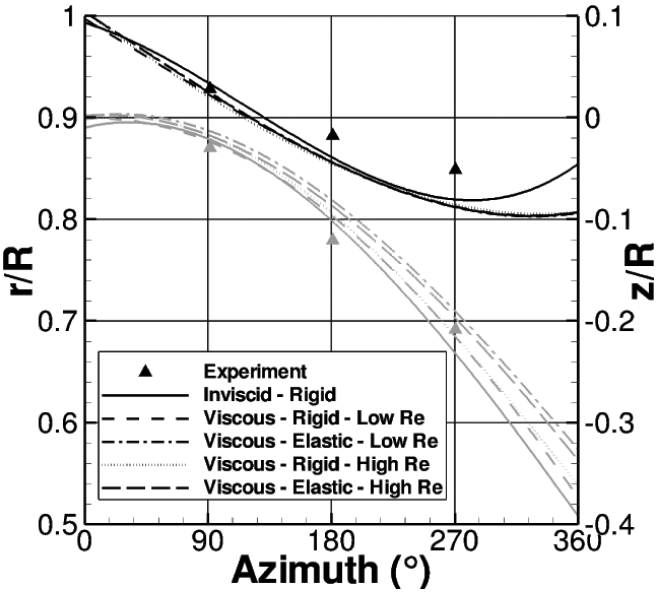


Figure 18. Vortex radial (black) and vertical (grey) location in the wake of hovering UH-60A model (low Re) and full-scale (high Re) rotors at C_T/σ = 0·170. Experiments by Lorber *et al*[18].

The lack of a comprehensive and widely available aeroelastic test case in hover did not allow for further validation of the results. An experimental data set containing both flow properties like pressure measurements, the vortex locations as well as structural properties and the in-flight blade shape would allow a more comprehensive validation of the coupling procedure.

The proposed coupling strategy is now under evaluation for forward flying rotors. While the mesh deformation is efficient and can be used for forward flying rotors, the current structural model needs modifications. The simplest approach would be to adopt a modal rotor blade representation and couple the aerodynamics and structural dynamics using weakly- or strongly-coupled methods, as frequently reported in the literature. Due to the currently-employed implicit scheme of the HMB solver, exchange of information between the fluid and solid domain would be necessary during the Newton iterations used between time steps to achieve a strongly-coupled algorithm. The overhead of this method is expected to be greater than what is reported here for hovering rotors. On the other hand, stability benefits during the unsteady simulation will out-weight the CPU penalty.

REFERENCES

1. MAIER, T.H., SHARPE, D.L. and LIM, J.W. Fundamental investigation of hingeless rotor aeroelastic stability, test data and correlation, 1998, 51st American Helicopter Society Forum, 9–11 May 1995, Fort Worth, TX, USA.
2. JOHNSON, W. Rotorcraft aerodynamics models for a comprehensive analysis, 1998, 54th American Helicopter Society Forum, 20–22 May 1998, Washington, DC, USA.
3. DEQUIN, A.M., BENOIT, B., KAMPA, K., VON GRŰNHAGEN, W., BASSET, P.M. and GIMONET, B. HOST, a general helicopter simulation tool for Germany and France, 2000, 56th American Helicopter Society Forum, 2-4 May 2000, Virginia Beach, VA, USA.

https://doi.org/10.1017/S0001924000007107 Published online by Cambridge University Press

4. POTSDAM, M., YEO, H. and JOHNSON, W. Rotor airloads prediction using loose aerodynamic/structural coupling, *J Aircr*, 2006, **43**, (3), pp 732–742.
5. LIM, J.C. AND STRAWN, R.C., Computational modeling of HART II blade-vortex interaction loading and wake system, *J Aircr*, **45**, (3), 2008, pp 923–933.
6. BIEDRON, R.T. and LEE-RAUSCH, E.M. Rotor airloads prediction using unstructured meshes and loose CFD/CSD coupling, 2008, AIAA-2008-7341, 26th AIAA Applied Aerodynamics Conference, 18–21 August 2008, Honolulu, HI, USA.
7. PAHLKE, K. and VAN DER WALL, B.G. Chimera simulations of multibladed rotors in high-speed forward flight with weak fluid-structure-coupling, *Aerospace Sci Tech*, 2005, **9**, (5), pp 379–389.
8. DIETZ, M., KESSLER, M. and KRÄMER, E. Aeroelastic simulations of isolated rotors using weak fluid-structure coupling, *High Performance Computing in Science and Engineering 06*, 2007, Springer Berlin Heidelberg.
9. BEAUMIER, P., ARNAUD, G. and CASTELLIN, C. Performance prediction and flowfield analysis of rotor in hover, using a coupled Euler/boundary layer method, *Aerospace Sci Tech*, 1999, **3**, (8), pp 473–484.
10. ALTMIKUS, A.R.M., WAGNER, S., BEAUMIER, P. and SERVERA, G. A comparison -weak versus strong modular coupling for trimmed aeroelastic rotor simulations, 2002, 58th American Helicopter Society Forum, 11–13 June 2002, Montreal, Canada.
11. SITARAMAN, J. and ROGET, B. Prediction of helicopter maneuver loads using a fluid-structure analysis, *J Aircr*, 2009, **46**, (5), pp 1770–1784.
12. POTSDAM, M., YEO, H. and JOHNSON,W. Rotor airloads prediction using loose aerodynamics/structural coupling, 2004, 60th American Helicopter Society Forum, 7–10 June 2004, Baltimore, MD, USA.
13. SCHMITZ, S., BHAGWAT, M., MOULTON, M.A., CARADONNA, F.X. and CHATTOT, J.-J. The predictions and validation of hover performance and detailed blade loads, 2009, *J American Helicopter Soc*, **54**, (1), pp 1–12.
14. YOON,S .-H., KWAK, J.S., SHIN, S. and KIM, C. Loosely coupled CFD/CSD analysis for a helicopter rotor in hover and forward flight, 2010, AHS Aeromechanics Specialists Conference 2010, 20–22 January 2010, San Francisco, CA, USA.
15. TRUONG, K.V. Dynamics studies of the ERATO blade, based on finite element analysis, 2005, 31th European Rotorcraft Forum, 13–15 September 2005, Florence, Italy.
16. DATTA, A. and JOHNSON, W. A multibody formulation for three dimensional brick finite elements based parallel and scalable rotor dynamic analysis, 2010, 66th American Helicopter Society Forum, 11–13 May 2010, Phoenix, AZ, USA.
17. THEPVONGS, S., COOK, J.R., CESNIK, C.E.S. and SMITH, M.J. Computational aeroelasticity of rotatingwings with deformable airfoils, 2009, 65th American Helicopter Society Forum, 27–29 May 2009, Grapevine, TX, USA.
18. LORBER, P.F., STAUTER, R.C. and LANDGREBE, A.J. A Comprehensive hover test of the airloads and airflow of an extensively instrumented model helicopter rotor, 1989, 45th American Helicopter Society Forum, 22–24 May 1989, Washington, Boston, MA, USA.
19. LORBER, P.F. Aerodynamic results of a pressure-instrumented model rotor test at the DNW, *J American Helicopter Soc*, 1991, **36**, (4), pp 12–19.
20. WAKE, B.E. and BAEDER, J.D. Evaluation of a Navier-Stokes analysis method for hover performance prediction, J American Helicopter Society, 1996, **41**, (1), pp 7–17.
21. SHINODA, P.M., YEO, H. and NORMAN, T.R. Rotor performance of a UH-60 rotor system in the NASA Ames 80- by 120-foot wind tunnel, *J American Helicopter Soc*, 2004, **49**, (4), pp 401–413.
22. BEAUMIER, P., CHELLI, E. and PAHLKE, K. Navier-Stokes predictions of helicopter rotor performance in hover including aeroelastic effects, *J American Helicopter Soc*, 2001, **46**, (4), pp 301–309.
23. OSHER, S. and CHAKRAVARTHY, S. Upwind schemes and boundary conditions with applications to Euler equations in general geometries, *J Computational Physics*, Jan–Feb 1983, **50**, pp 447–481.
24. AXELSSON, O. *Iterative Solution Methods*, 1994, Cambridge University Press, Cambridge, MA, USA.
25. STEIJL, R., BARAKOS, G. and BADCOCK, K. A framework for CFD analysis of helicopter rotors in hover and forward flight, *Int J Numerical Methods in Fluids*, 2006, **51**, (8), pp 819–847.
26. DUBUC, L., CANTARITI, F., WOODGATE, M.A., GRIBBEN, B., BADCOCK, K.J. and RICHARDS, B.E. A grid deformation technique for unsteady flow computations, *Int J Numerical Methods in Fluids*, 2000, **32**, (3), pp 285–311.
27. ARCIDIACONO, P. and ZINCONE, R. Titanium UTTAS main rotor blade, *J American Helicopter Soc*, 1976, **21**, (2), pp 12–19.

https://doi.org/10.1017/S0001924000007107 Published online by Cambridge University Press

28. VAN DER WALL, B.G., BURLEY, C.L., YU, Y., RICHARD, H., PENGEL, K. and BEAUMIER, P. The HART II test measurement of helicopter rotor wakes, *Aerospace Sci Tech*, 2004, **8**, (4), pp 273–284.
29. HO, J.C., YEO, H. and ORMISTON, R.A. Investigation of rotor blade structural dynamics and modeling based on measured airloads, *J Aircr*, 2008, **45**, (5), pp 1631–1642.
30. HAMADE, K.S. and KUFELD, R.M. Modal analysis of UH-60A instrumented rotor blades, 1990, NASA Technical Report, TR-4239, NASA.
31. GOURA, G.S.L., BADCOCK, K.J., WOODGATE, M.A. and RICHARDS, B.E. Implicit method for the time marching analysis of flutter, *Aeronaut J*, 2001, **105**, (1046), pp 199–214.
32. BLOM, F.J., Considerations on the spring analogy, *Int J Numerical Methods in Fluids*, 2000, **32**, (6), pp 647–668.
33. MENTER, F.R. Two-equation eddy-viscosity turbulence models for engineering applications, *AIAA J*, 1994, **32**, (8), pp 1598–1605.
34. KIM, K.C. Analytical calculations of helicopter torque coefficient (CQ) and thrust coefficient (CT) values for the helicopter performance (HELPE) model, 1999, Army Research Laboratory Technical Report, ARL-TR-1986, Army Research Laboratory.
35. ORTUN, B., PETOT, D., TRUONG, K.V. and OHAYON, R. Towards a new generation of rotorcraft comprehensive analysis; coupling with CSM and CFD, 2008, 34th European Rotorcraft Forum, 16–18 September 2008, Liverpool, UK.

https://doi.org/10.1017/S0001924000007107 Published online by Cambridge University Press

NATIONAL AEROSPACE LIBRARY

ROYAL AERONAUTICAL SOCIETY

THE NATIONAL AEROSPACE LIBRARY FARNBOROUGH

LOCATED AT FARNBOROUGH IQ BUSINESS PARK IN THE FORMER ROYAL AIRCRAFT ESTABLISHMENT BUILDING NOW KNOWN AS 'THE HUB'





Available to view at the National Aerospace Library are:

- Over 20,000 aeronautical books
- A vast collection of key aviation journals
- Over 40,000 technical reports
- Extensive holdings of Air Publications, ATA handling notes and air accident reports
- Extensive current holdings of International Civil Aviation Organization (ICAO) Documents / Annexes / Circulars
- Notices to Airmen / The Air Pilot / UK Aeronautical Information Publication (AIP)
- A complete set of Jane's All The World's Aircraft
- Historically important past minutes of the Society of British Aircraft Constructors / Aerospace Companies (SBAC) Council and its various committees dating from 1916-2000
- Extensive online database

www.aerosociety.com/nal

The National Aerospace Library
The Hub, Fowler Avenue,
IQ Farnborough,
Farnborough, Hants GU14 7JP
United Kingdom

Tel: +44 (0)1252 701038
Email: hublibrary@aerosociety.com
www.aerosociety.com/nal

Opening hours
Tuesday - Friday 10:00 - 16:00

https://doi.org/10.1017/S0001924000007107 Published online by Cambridge University Press